HIV-1 budding requires cortical actin disassembly by the oxidoreductase MICAL1

Thomas Serrano[a,1] [iD], Nicoletta Casartelli[b,1] [iD], Foad Ghasemi[c] [iD], Hugo Wioland[c] [iD], Frédérique Cuvelier[a], Audrey Salles[d] [iD], Maryse Moya-Nilges[e], Lisa Welker[f,g] [iD], Serena Bernacchi[f] [iD], Marc Ruff[g] [iD], Antoine Jégou[c], Guillaume Romet-Lemonne[c] [iD], Olivier Schwartz[b], Stéphane Frémont[a,2,3] [iD], and Arnaud Echard[a,2,3] [iD]

Affiliations are included on p. 11.

Many enveloped viruses bud from the plasma membrane that is tightly associated with a dense and thick actin cortex. This actin network represents a significant challenge for membrane deformation and scission, and how it is remodeled during the late steps of the viral cycle is largely unknown. Using superresolution microscopy, we show that HIV-1 buds in areas of the plasma membrane with low cortical F-actin levels. We find that the cellular oxidoreductase MICAL1 locally depolymerizes actin at budding sites to promote HIV-1 budding and release. Upon MICAL1 depletion, F-actin abnormally remains at viral budding sites, incompletely budded viruses accumulate at the plasma membrane and viral release is impaired. Remarkably, normal viral release can be restored in MICAL1-depleted cells by inhibiting Arp2/3-dependent branched actin networks. Mechanistically, we find that MICAL1 directly disassembles branched-actin networks and controls the timely recruitment of the Endosomal Sorting Complexes Required for Transport scission machinery during viral budding. In addition, the MICAL1 activator Rab35 is recruited at budding sites, functions in the same pathway as MICAL1, and is also required for viral release. This work reveals a role for oxidoreduction in triggering local actin depolymerization to control HIV-1 budding, a mechanism that may be widely used by other viruses. The debranching activity of MICAL1 could be involved beyond viral budding in various other cellular functions requiring local plasma membrane deformation.

HIV-1 budding | actin | Arp2/3 | MICAL1 | ESCRT

Significance

Viruses hijack cellular mechanisms to replicate and thus propagate. To produce infectious particles, enveloped viruses like HIV-1 must deform and scission the plasma membrane of infected cells. This membrane is associated with a dense and thick actin cortex that represents a barrier for membrane deformation. Here, we find that the cellular oxidoreductase MICAL1 and its activator the GTPase Rab35 promote the release of viruses through the disassembly of actin filaments at budding sites. This work reveals an unexpected connection between oxidoreduction and viral budding.

The plasma membrane undergoes continuous remodeling to ensure cellular events such as endocytosis, exocytosis, cell division, or viral budding. The egress of enveloped viruses from infected cells and the final step of cell division—cytokinetic abscission—require membrane deformation and topologically equivalent scission events mediated by the same cellular endosomal sorting complexes required for transport (ESCRT) machinery (1–10). Whether other mechanisms are shared during cytokinetic abscission and viral budding remains largely unexplored.

HIV-1 budding involves coordinated interactions between viral proteins and the plasma membrane (11–13). The viral Gag polyprotein plays a crucial role by orchestrating virus assembly, budding, and release. Gag polyproteins first bind to the plasma membrane and then cluster into PtdIns(4, 5)P2-rich domains to generate viral particles in which viral RNA is packaged. Finally, Gag recruits the ESCRT machinery required for membrane scission and viral release from the infected cell.

Below the plasma membrane, the actin cortex forms a 200 nm-thick, dense, and cross-linked meshwork of actin filaments (14–17). The actin cortex and its tight association with the plasma membrane represents a significant challenge for membrane deformation and scission during the final steps of the HIV-1 cycle. Several studies have reported an active role for actin dynamics in the assembly and budding of HIV-1 (18–22) while others have argued against it (23, 24). While the exact role of the actin cortex in the late steps of the HIV-1 cycle remains debated (25), it is likely that membrane deformability and scission depend on actin dynamics at virus assembly and budding sites. In particular, the potential interplay between the actin cytoskeleton and the ESCRT-III machinery during budding is unknown.

During cytokinesis, the clearance of actin filaments (F-actin) from the intercellular bridge (ICB) connecting the two daughter cells is required for the scission of the plasma membrane and thus successful abscission (26–34). We previously demonstrated that the oxidoreductase Molecule interacting with CasL protein 1 (MICAL1)—an enzyme that accelerates actin filament disassembly—is recruited and activated in the ICB by the small Guanosine Tri

Phosphatase (GTPase) Rab35 to locally depolymerize actin filaments, thus promoting cytokinetic abscission (34). MICAL1 belongs to a conserved family of flavoenzyme oxidoreductases named MICAL that directly oxidize specific methionine residues in actin filaments, leading to their rapid disassembly (35–39). Mechanistically, actin disassembly by MICAL1 promotes ESCRT-III localization at the abscission site and thus membrane scission (34).

Here, we hypothesized that cortical actin filaments are similarly depolymerized by Rab35/MICAL1 during HIV-1 budding at the plasma membrane to facilitate the ESCRT-III-dependent release of viruses from infected cells. We found that HIV-1 budding preferentially occurs in regions of the plasma membrane with reduced F-actin levels. In contrast, F-actin remains at high levels at budding sites in the absence of MICAL1, whose depletion induces an accumulation of incompletely budded viral particles at the plasma membrane and delays ESCRT-III recruitment at budding sites, leading to impaired HIV-1 release from infected cells. Finally, our results indicate that MICAL1 and its activator Rab35 function in the same pathway during HIV-1 budding and release. Altogether, this work reveals a role for oxidoreduction in retroviral budding, linking MICAL-1-mediated oxidation to local actin depolymerization at HIV-1 budding sites.

Results

MICAL1 Depletion Reduces HIV-1 Release From Infected Cells. We first investigated the role of MICAL1 in the late stages of the HIV-1 cycle over one single viral cycle. To this aim, we silenced MICAL1 in HeLa cells using a specific small interfering RNA (siRNA) and then infected the cells with the HIV-1 strain NL4-3 pseudotyped with the vesicular stomatitis virus G glycoprotein (NL4-3-VSVG). Treatment with MICAL1 siRNAs led to an efficient depletion of MICAL1 in infected cells (*SI Appendix,* Fig. S1*A*). The day after infection, we exchanged the media to remove residual viral input and let cells produce viruses for 24 h. Viral proteins both in infected cells and released in the supernatant were then analyzed by Western Blot (WB) using anti-Gag antibodies (Fig. 1*A*). The levels of Gag-p24 in the supernatant were reduced after MICAL1 depletion, with no decrease in the intracellular Gag precursor (Gag-p55) and Gag subproducts (Gag-p41+Gag-p24) levels. We then quantified the levels of Gag-p24 in both the supernatant and infected cells by enzyme-linked immunosorbent assay (ELISA). MICAL1 depletion resulted in a 60 ± 16% reduction of HIV-1 release (Fig. 1*B*). These results were confirmed with a second siRNA targeting MICAL1 (*SI Appendix,* Fig. S1 *B* and *C*). We conclude that MICAL1 is required for efficient release of HIV-1 from infected cells.

To determine when the release of the virus starts to be affected by the MICAL1 depletion, we monitored the kinetics of Gag-p24 release in the supernatant of infected cells. Twenty-four hours post-infection, we replaced the culture medium with fresh medium and collected viral supernatants at 4 – 6 – 8 and 24 h and measured Gag-p24 by ELISA. At the end of the experiment, we collected infected cells and found that cell-associated Gag-p24 levels were unchanged in MICAL1-depleted cells, (*SI Appendix,* Fig. S1*D*). In contrast, the amounts of Gag-p24 in the supernatant were reduced in MICAL1-depleted cells at all time points (Fig. 1*C*), suggesting that HIV-1 release is impaired as soon as the infected cells start to produce viruses. Of note, MICAL1 depletion affected the release of both immature (Gag-p55) and mature (Gag-p24) as shown by WB analysis of purified viruses (*SI Appendix,* Fig. S1*E*).

We next investigated whether the maturation and the infectivity of the released viruses were affected by MICAL1 depletion. First, we analyzed virion maturation by transmission electron microscopy

(TEM) and classified virions as either immature—characterized by discernible immature Gag shells—or mature—characterized by discernible conical or condensed cores (Fig. 1*D*). In control cells, 87% of the released virions were mature (n = 232 virions). Similar results were obtained in MICAL1-depleted cells (90% mature, n = 165 virions) (Fig. 1*D*). We next used the HeLa P4C5 reporter cells to assess viral infectivity after infection with equal amounts of viral particles. We observed that infectivity of the released viruses was unchanged after MICAL1 depletion (Fig. 1*E*). Thus, MICAL1 depletion reduces HIV-1 release but does not perturb viral maturation or subsequent infectivity.

To confirm the role of MICAL1 during viral release in a cell type naturally infected by HIV-1, we depleted MICAL1 in monocyte-derived macrophage THP-1 cells and infected them overnight with NL4-3-VSVG viruses. We then replaced the culture medium with fresh medium and collected the virus produced over the next 48 h. We observed that the levels of Gag-p24 in the supernatant were reduced after MICAL1 depletion, as assessed by WB (Fig. 1*F*). We quantified the viral release by Gag-p24-ELISA and found that MICAL1 depletion in THP-1 cells resulted in a 37 ± 21% reduction of HIV-1 release (Fig. 1*G*).

We finally investigated potential interactions between MICAL1 and Gag using immunoprecipitation assays. We infected HeLa cells with the NL4-3-VSVG virus, immunoprecipitated endogenous MICAL1, and found that it coimmunoprecipitated Gag-p55 (Fig. 1*H*). To confirm this interaction, we transfected HeLa cells with a NL4-3-Gag-GFP provirus, immunoprecipitated Gag-GFP, and found that it coimmunoprecipitated endogenous MICAL1 (*SI Appendix,* Fig. S1*F*). These results indicate that MICAL1 and Gag form a complex and show that MICAL1 functions during viral budding and/or release.

MICAL1 Depletion Induces Accumulation of HIV-1 Budding Particles at the Plasma Membrane. Reduction of viral particle release can result from a defect during the budding process, leading to the accumulation of viruses at the plasma membrane of infected cells. We first analyzed the distribution of Gag and Env (viral envelope glycoprotein) structural proteins using spinning disk confocal microscopy 36 h after NL4-3-VSVG infection in HeLa cells, both in the absence or presence of MICAL1. As expected, we observed a colocalization of the Gag and Env signals at the plasma membrane in both conditions (Fig. 2*A* and *SI Appendix,* Fig. S2*A*).

Automatic detection of Gag-positive regions (*SI Appendix,* Fig. S2 *B*, *Top*) revealed that MICAL1 depletion induced an increase in both the number and the surface of individual Gag-positive regions resulting in an increase of the total area covered by the Gag staining (Fig. 2*B* and *SI Appendix,* Fig. S2 *B*, *Bottom*). These results indicate that MICAL1 depletion induces the formation of larger and more numerous Gag/Env regions at the plasma membrane, suggesting an accumulation of budding viruses at the cell surface.

This was confirmed by visualizing single viral particles on the surface of infected cells, using correlative light scanning electron microscopy (SEM) in HeLa cells infected with a NL4-3-Gag-GFP virus (Fig. 2*C*). We observed a twofold increase in the density of viruses at Gag-GFP-positive budding regions in MICAL1-depleted cells, as compared to control cells (Fig. 2*D*).

Altogether, these results show that MICAL1 depletion induces accumulation of budding viruses at the surface of infected cells, which likely accounts for the defective viral release observed in MICAL1-depleted cells.

MICAL1 Depletion Impairs Normal Budding and Delays ESCRT-III Recruitment at Budding Sites. The accumulation of budding viruses in MICAL1-depleted cells suggests incomplete viral budding
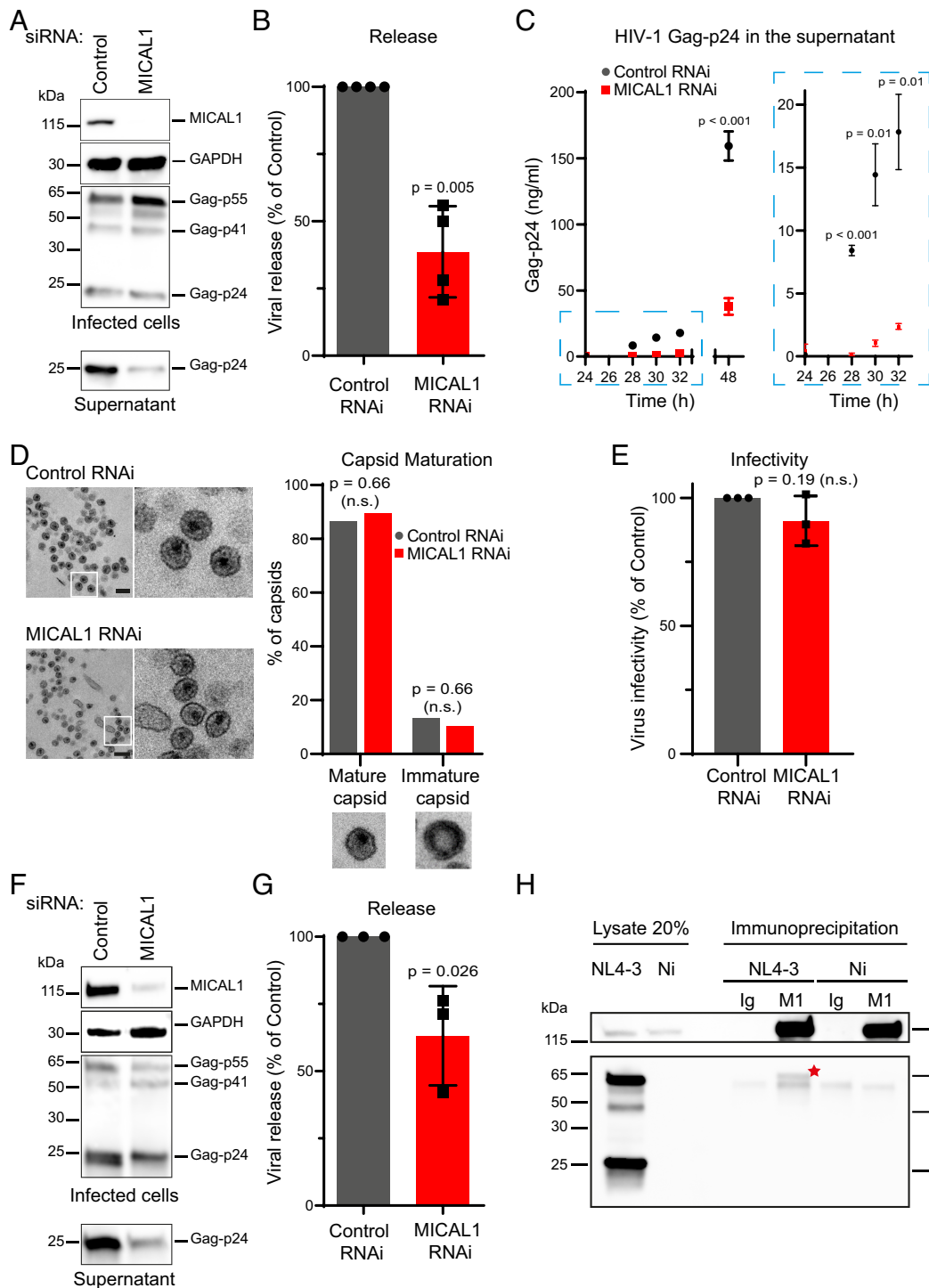
Fig. 1. MICAL1 depletion reduces HIV-1 release from infected cells. (*A*) WB analysis of HIV-1 Gag products in infected HeLa cells treated with indicated siRNAs (panels Infected cells) and corresponding supernatants (panel Supernatant). Loading control: GAPDH. Equal volumes of cell and supernatant samples were loaded. This experiment was repeated at least three times independently with similar results. (*B*) Quantification by Gag-p24 ELISA of HIV-1 release in HeLa cells treated with either Control or MICAL1 siRNAs. Results were normalized to control RNAi conditions (set at 100%). Error bars represent SD calculated from 4 independent experiments, each done in triplicate. Two-tailed unpaired Student's *t* test. (*C*) Quantification by ELISA of released Gag-p24 in the supernatant of infected HeLa cells treated with either Control or MICAL1 siRNAs at indicated times after infection. Error bars represent SD calculated from one experiment done in triplicate. Two-tailed unpaired Student's *t* test. (*D*, *Left*) Transmission electron microscopy images of released viruses from infected HeLa cells treated with either Control or MICAL1 siRNAs. (Scale bars, 200 nm.) (*Right*) Quantification of the proportion of mature vs. immature capsids. n = 232 (Control RNAi) and n = 165 (MICAL1 RNAi) released capsids. Fisher's exact test. (*E*) The virus infectivity was scored by measuring beta-galactosidase levels in infected HeLa P4C5 reporter cells treated with either Control or MICAL1 siRNAs. The beta-galactosidase values were normalized to the amount of released Gag-p24. Results were normalized to control RNAi conditions (set at 100%). Error bars represent SD calculated from three independent experiments. Two-tailed unpaired Student's *t* test. (*F*) WB analysis of HIV-1 Gag products in infected THP-1 cells treated with indicated siRNAs (panels Infected cells) and corresponding supernatants (panel Supernatant). Loading control: GAPDH. Equal volumes of cell and supernatant samples were loaded. This experiment was repeated at least three times independently with similar results. (*G*) Quantification by Gag-p24 ELISA of HIV-1 release in THP-1 cells treated with either Control or MICAL1 siRNAs. Results were normalized to control RNAi conditions (set at 100%). Error bars represent SD calculated from three independent experiments, each done in triplicate. Two-tailed unpaired Student's *t* test. (*H*) Endogenous MICAL1 from infected (NL4-3) or noninfected (Ni) HeLa cells was revealed with anti-MICAL1 antibodies (control immunoprecipitation = Rabbit IgG). Coimmunoprecipitated Gag-p55 (red star) was revealed with anti-Gag antibodies. The lower band corresponds to nonspecific background also present in noninfected cells.
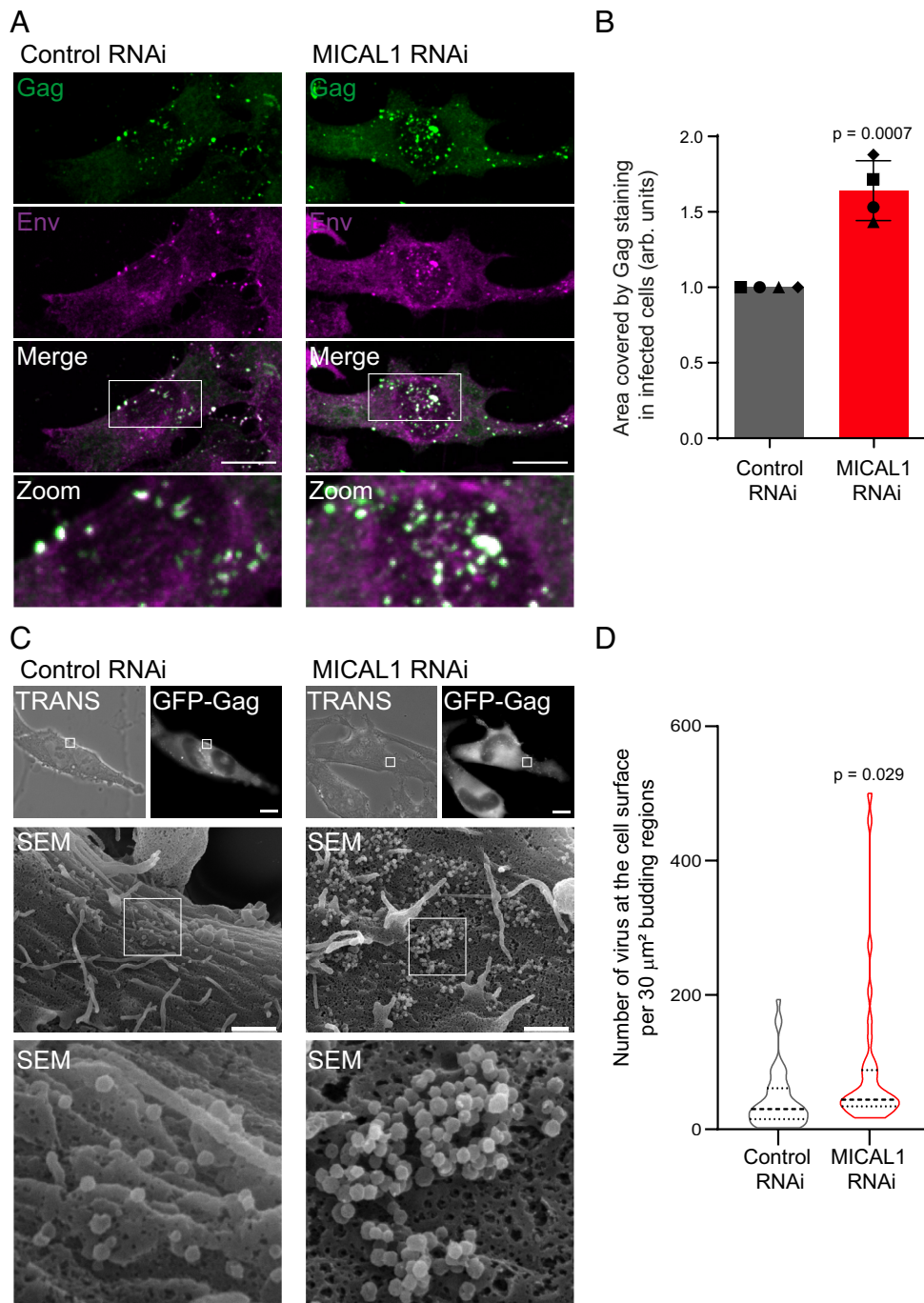
Fig. 2. MICAL1 depletion induces accumulation of HIV-1 budding particles at the plasma membrane. (*A*) Z projection of spinning disk confocal images of infected HeLa cells treated with indicated siRNAs and labeled with anti-Gag (green) and anti-Env (magenta) antibodies. (Scale bars, 10 μm.) (*B*) Quantification of the area covered by Gag staining in infected cells (arbitrary units, arb. units). Results were normalized to control RNAi conditions (set at 1.0) Error bars represent SD calculated from four independent experiments. n = 145 (Control RNAi) and n = 154 (MICAL1 RNAi) cells analyzed. Two-tailed unpaired Student's *t* test. (*C*) Correlative light-scanning electron microscopy (SEM) of HeLa cells transfected with NL4-3-Gag-GFP provirus after control (*Left*) or MICAL1 (*Right*) depletion. Phase-contrast (TRANS), fluorescent, and SEM pictures with corresponding zooms of budding regions are presented. (Scale bars, 10 μm for fluorescence pictures and 1 μm for SEM.) (*D*) Quantification of the number of viruses at the cell surface per 30 μm² budding regions (violin plot with median and interquartiles). n = 47 budding regions from 13 cells analyzed in Control RNAi conditions and n = 35 budding regions from nine cells analyzed in MICAL1 RNAi conditions. Kolmogorov–Smirnov test.

and/or defective scission. Incomplete viral budding results in the accumulation of budding events with a characteristic "half-moon" shape (40, 41). Conversely, a defect in viral particle scission leads to the formation of a typical "lollipop" shape budding particles (42). Analysis of TEM images from MICAL1-depleted cells infected with NL4-3-VSVG revealed an accumulation of incompletely budded viruses at the plasma membrane (Fig. 3*A*). Budding virions in MICAL1-depleted cells displayed decreased height (72 ± 33 nm, n = 134), as compared to control cells (99 ± 25 nm, n = 132),

while the width was similar (133 ± 25 nm and 129 ± 22 nm in control and in MICAL1-depleted cells, respectively) (Fig. 3*B*). Consequently, the height-to-width ratio decreased by 32% in MICAL1-depleted cells (Fig. 3*B*). Thus, MICAL1 depletion leads to the accumulation of incomplete budded particles at the plasma membrane.

We next investigated whether MICAL1 depletion impaired the recruitment of the ESCRT-III protein CHMP4B at budding sites. First, infected control and MICAL1-depleted cells were stained
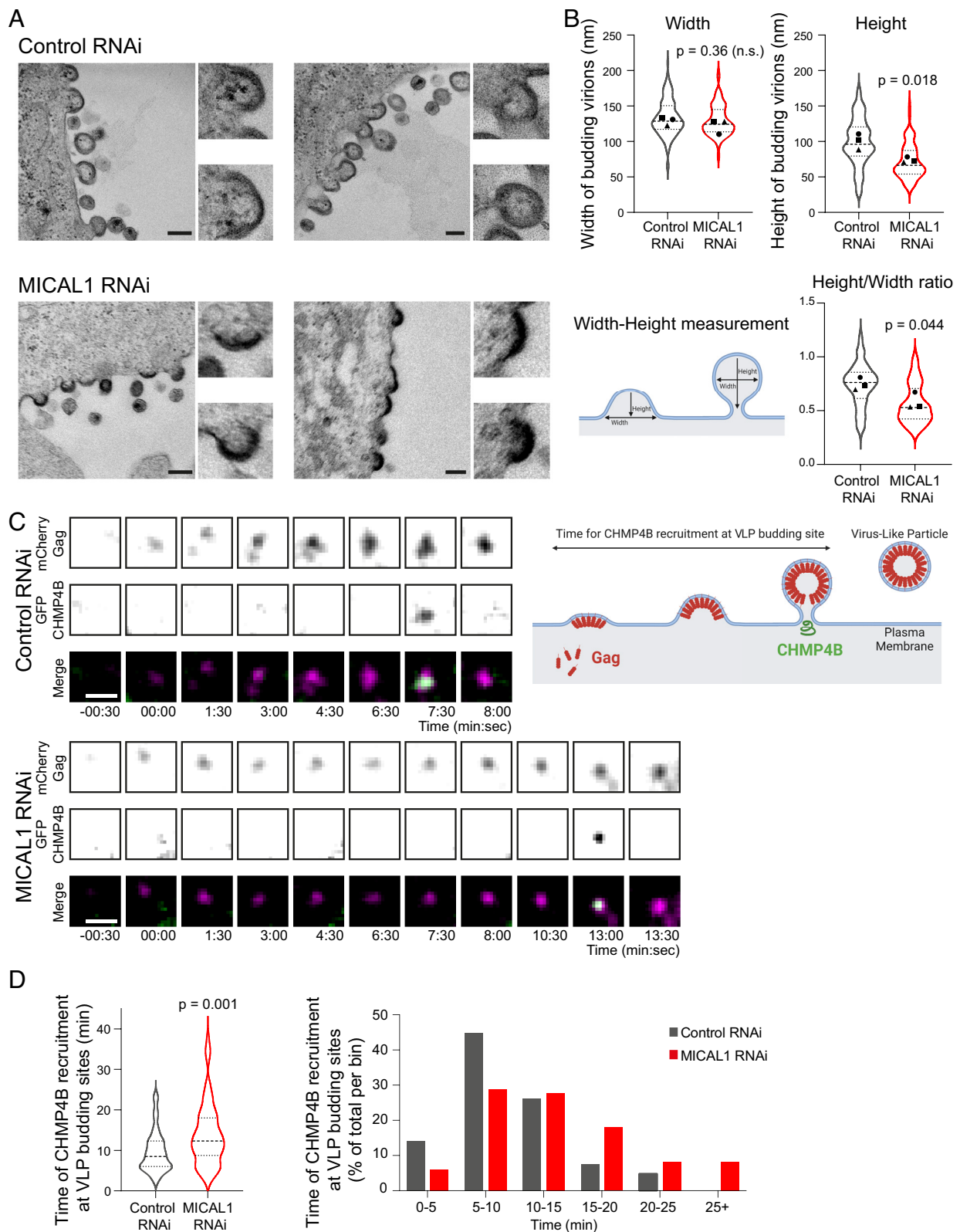
Fig. 3. MICAL1 depletion impairs normal budding and delays ESCRT-III recruitment at budding sites. (*A*) TEM of infected HeLa cells treated with either Control or MICAL1 siRNAs. (Scale bars, 200 nm.) (*B*) Width, Height, and Height/Width ratio of budding virions in infected HeLa cells treated with either Control or MICAL1 siRNAs. Mean of three independent experiments (violin plot with median and interquartiles). n = 132 (Control RNAi) and n = 134 (MICAL1 RNAi) buds. Two-tailed unpaired Student's *t* test. (*C*) Time-lapse images (one image every 30 s for 45 min) using TIRF microscopy of HeLa cells stably expressing GFP-CHMP4B (green) and transfected with plasmid encoding Gag-mCherry (magenta) after treatment with either Control or MICAL1 siRNAs. (Scale bars, 1 μm.) (*D*) Quantification of the time of CHMP4B recruitment at VLP budding sites. (*Left*) Violin plot with median and interquartiles. (*Right*) Histograms of distribution of CHMP4B recruitment times. n = 75 VLPs from eight cells and 92 VLPs from eight cells in Control RNAi and MICAL1 RNAi conditions, respectively. N = 3 independent experiments. Kolmogorov–Smirnov test.

with anti-Gag and anti-CHMP4B antibodies and analyzed by spinning disk microscopy to quantify the percentage of colocalization between these two proteins (*SI Appendix,* Fig. S2C). In Gag-positive regions of control cells, 40% of the Gag-positive pixels colocalized with CHMP4B. In the absence of MICAL1, this percentage was significantly reduced to 26% (*SI Appendix,* Fig. S2C). This suggests that MICAL1 promotes CHMP4B recruitment to the budding regions. We then performed total internal reflection fluorescence (TIRF) microscopy in HeLa cells stably expressing GFP-tagged CHMP4B (43) and transfected with a plasmid encoding a carboxy-terminally tagged Gag (Gag-mCherry), leading to the formation of virus-like particles (VLPs) that bud at the plasma membrane (44). By tracking Gag and CHMP4B kinetics with time-lapse microscopy, we determined the time for CHMP4B recruitment at VLP budding sites (Fig. 3C and *SI Appendix,* Fig. S2D). In the representative examples presented in Fig. 3C, the mCherry signal gradually accumulates until GFP-CHMP4B is recruited at the budding site after 7 min 30 s in control cell vs. 13 min in MICAL1-depleted cell (T0 being the first time point where we could detect a mCherry-Gag spot at the plasma membrane). The analysis of 75 to 92 budding events where CHMP4B was recruited showed that CHMP4B recruitment occurred 9.6 ± 5 min after Gag arrival in control cells (Fig. 3D), similarly to what has been previously observed (45). In contrast, the time necessary to recruit CHMP4B following Gag appearance was increased by 45% to 13.9 ± 7 min in MICAL1-depleted cells (Fig. 3D). Thus, CHMP4B recruitment at the budding site is delayed in MICAL1-depleted cells.

MICAL1 Depletion Impairs F-Actin Clearance at HIV-1 Budding Sites. Since MICAL1 binds and disassembles actin filaments, we hypothesized that MICAL1 depletion could affect F-actin levels at HIV-1 budding sites. Using spinning disk confocal microscopy, we observed that, in control cells, F-actin levels—visualized by fluorescent phalloidin—were reduced in Gag-positive regions of the plasma membrane, compared to adjacent Gag-negative regions (Fig. 4 A, *Left* and Fig. 4B). In contrast, in MICAL1-depleted cells, F-actin levels in Gag-positive regions remained as high as in Gag-negative regions (Fig. 4 A, *Right* and Fig. 4B). We next classified the budding regions into three categories based on F-actin intensity in Gag-positive regions compared to adjacent Gag-negative regions: 1) reduced F-actin in Gag-positive regions (at least 30% reduced intensity), 2) increased F-actin in Gag-positive regions (at least 30% increased intensity), and 3) no significant differences in F-actin levels (between 30% reduced intensity and 30% increased intensity). In control cells, 60% of budding regions localized in areas of reduced F-actin while in MICAL1-deficient cells, this was observed in only 39% of budding regions (Fig. 4C). Furthermore, in MICAL1-depleted cells, there was a significant increase in budding regions localized in areas where F-actin levels were similar to nearby regions (Fig. 4C). We confirmed in Jurkat T cells and activated primary CD4 T cells infected with the NL4-3-VSVG virus that HIV-1 budding occurred mainly in the regions of the plasma membrane where cortical actin was reduced (in 60.8% in Jurkat T cells and in 57.4% in primary CD4 T cells) (*SI Appendix,* Fig. S3 A and B). This is consistent with a recent report showing that Gag assembly occurs in less dense F-actin area at the T cell plasma membrane (22).

To visualize the cortex underneath budding sites at high resolution, we turned to superresolution microscopy using two-color three-dimensional stochastic optical reconstruction microscopy (3D-STORM). We did not detect F-actin beneath most budding viruses in control cells (Fig. 4 D, *Left* and Fig. 4E). In contrast,

F-actin was present beneath budding viruses after MICAL1 depletion (Fig. 4 D, *Right* and Fig. 4E).

Altogether, these results indicate that HIV-1 buds preferentially in areas of the plasma membrane with relatively low cortical F-actin levels, and reveal that MICAL1 is key for locally clearing cortical actin at budding regions.

Inhibiting Branched-Actin Nucleation Restores Normal HIV-1 Release in MICAL1-Depleted Cells. The results above imply that decreasing F-actin levels at the cell cortex is required for efficient viral budding and release. We thus investigated whether the defects in viral release found in MICAL1-depleted cells could be rescued by inhibiting F-actin nucleation. To do so, we treated infected cells with the actin related protein 2/3 complex (Arp2/3) inhibitor CK666 (75 μM) to reduce the formation of branched F-actin networks. We first checked that the CK666 treatment at this concentration did not alter MICAL1 depletion (*SI Appendix,* Fig. S4A), did not impact cell viability (*SI Appendix,* Fig. S4B), and did not significantly affect HIV-1 release in control cells (Fig. 5A). Remarkably, CK666 treatment in MICAL1-depleted cells restored HIV-1 release (Fig. 5A) and the total area of budding regions (*SI Appendix,* Fig. S4C and quantified in Fig. 5B) to levels comparable to those observed in control, nondepleted cells. Thus, reducing branched-actin levels restores normal HIV-1 release in MICAL1-depleted cells. Furthermore, these results indicate that the abnormal persistence of F-actin at HIV-1 budding sites resulting from MICAL1 depletion is likely responsible for the defects in virus release.

MICAL1 Exhibits Debranching Activity. The CK666 rescue experiments also suggest that MICAL1 promotes the disassembly of branched actin networks. Yet, such a debranching activity of MICAL1, beyond its known function in actin disassembly, has not been investigated so far. We thus tested in vitro whether MICAL1 can promote the dissociation of F-actin branches, using fluorescence microscopy and purified proteins to monitor individual events in controlled conditions. To specifically characterize this activity on actin branches, we prevented barbed end depolymerization by ensuring sufficient levels of nonoxidized G-actin. First, we monitored the dissociation of actin filament branches in the absence of mechanical forces. We found that debranching occurred more rapidly in the presence of the monooxygenase catalytic domain of MICAL1 (MICAL1$^{1-499}$) and its coenzyme nicotinamide adenine dinucleotide phosphate (NADPH) (Fig. 5C). Since oxidation of F-actin by MICAL1 can favor the severing of filaments by weakening intrafilamentary bonds (46), we verified that the observed debranching was not due to severing of the oxidized filaments in our experiments (*SI Appendix,* Fig. S4D). As cortical F-actin branches are likely exposed to mechanical stress at the cell cortex, we then asked whether MICAL1 would also promote debranching under pulling forces. We thus monitored branch dissociation using microfluidics (47), which enables the application of a controlled pulling force to branched filaments (48). As previously reported (48, 49), the application of mechanical force alone accelerated branch dissociation (Fig. 5D, gray curves). In addition, the presence of MICAL1 strongly accelerated debranching, in a dose-dependent manner (Fig. 5D, red and blue curves). The presence of purified Gag did not modify the debranching activity of MICAL1 in vitro (*SI Appendix,* Fig. S4E), consistent with the absence of direct interaction between Gag and MICAL1 in two-hybrid assays (*SI Appendix,* Fig. S4F). Since we recently discovered that the Arp2/3 complex remains bound to the mother filament and nucleates a new branch following most branch dissociation events (48), we also monitored the impact of MICAL1 on
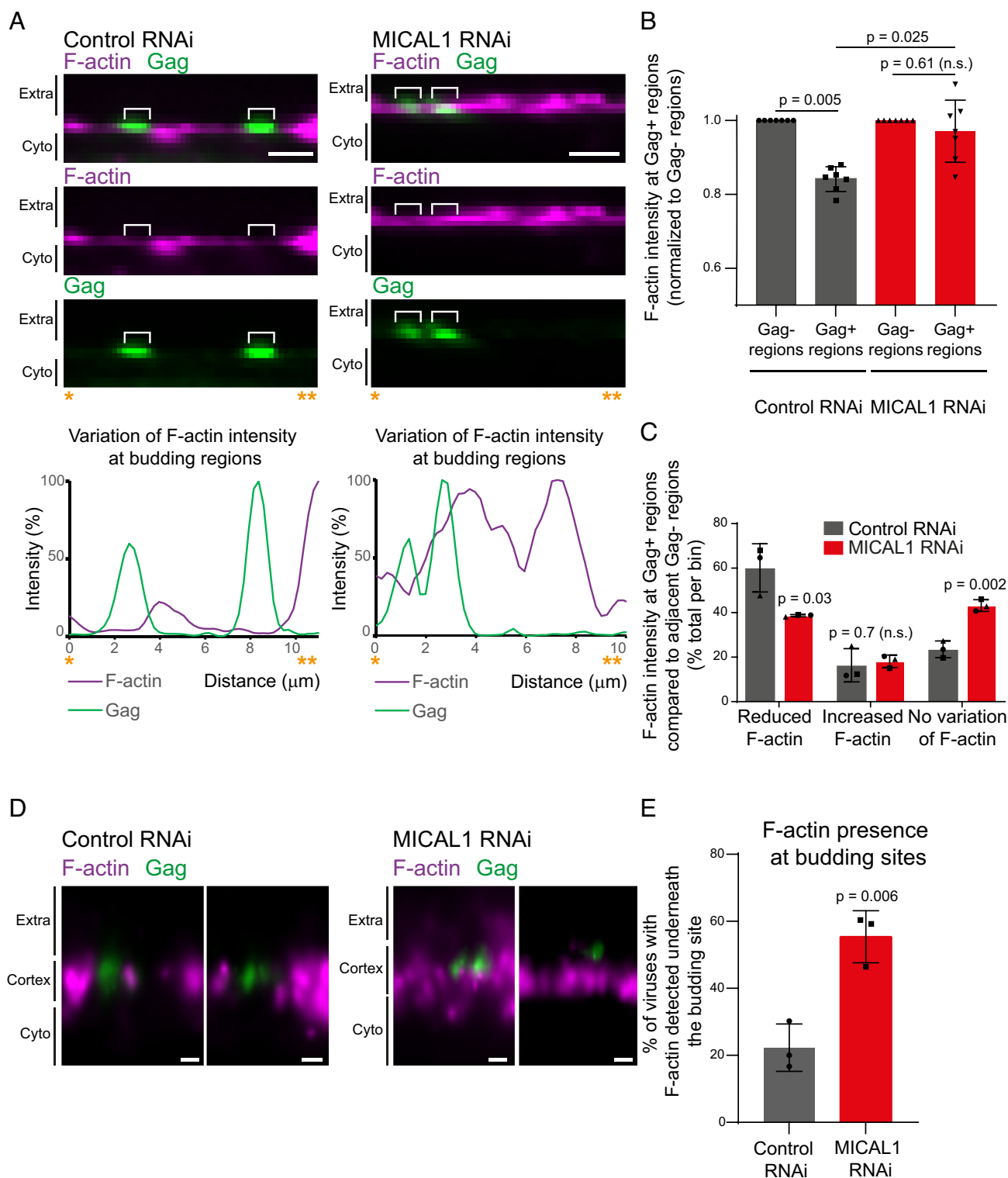
Fig. 4. MICAL1 depletion impairs F-actin clearance at HIV-1 budding sites. (*A*, *Top*) Spinning disk confocal images of infected HeLa cells treated with either Control (*Left*) or MICAL1 (*Right*) siRNAs and labeled with anti-Gag (green) antibody and fluorescent phalloidin (magenta). Extra: Extracellular space. Cyto: cytoplasm. (*Bottom*) Plot profile of the Gag and Phalloidin intensity of corresponding images. (Scale bars, 2 µm.) (*B*) Quantification of F-actin intensity (using fluorescent phalloidin) at Gag-positive (Gag+) and Gag-negative (Gag–) regions (normalized to Gag- regions), in Control and MICAL1-depleted HeLa cells (n = 132 and n = 154 Gag+ budding regions from seven cells analyzed in Control RNAi and MICAL1 RNAi conditions, respectively). Error bars represent SD. Two way-ANOVA multiple comparisons. (*C*) Quantification of the variations of F-actin intensity in Gag+ regions compared to adjacent Gag- regions. n = 176 Gag+ regions and n = 196 Gag+ regions from 12 cells analyzed in Control and MICAL1 RNAi conditions, respectively. Error bars represent SD calculated from three independent experiments. Two-tailed unpaired Student's *t* test. (*D*) 3D-STORM images of infected HeLa cells treated with either Control (*Left*) or MICAL1 (*Right*) siRNAs and labeled with anti-Gag antibody (green) and fluorescent phalloidin (magenta). (Scale bars, 200 nm.) (*E*) Quantification of F-actin presence at budding sites using 3D-STORM images. n = 74 and n = 98 budding viruses from three cells analyzed in Control RNAi and MICAL1 RNAi conditions, respectively. Error bars represent SD. Two-tailed unpaired Student's *t* test.
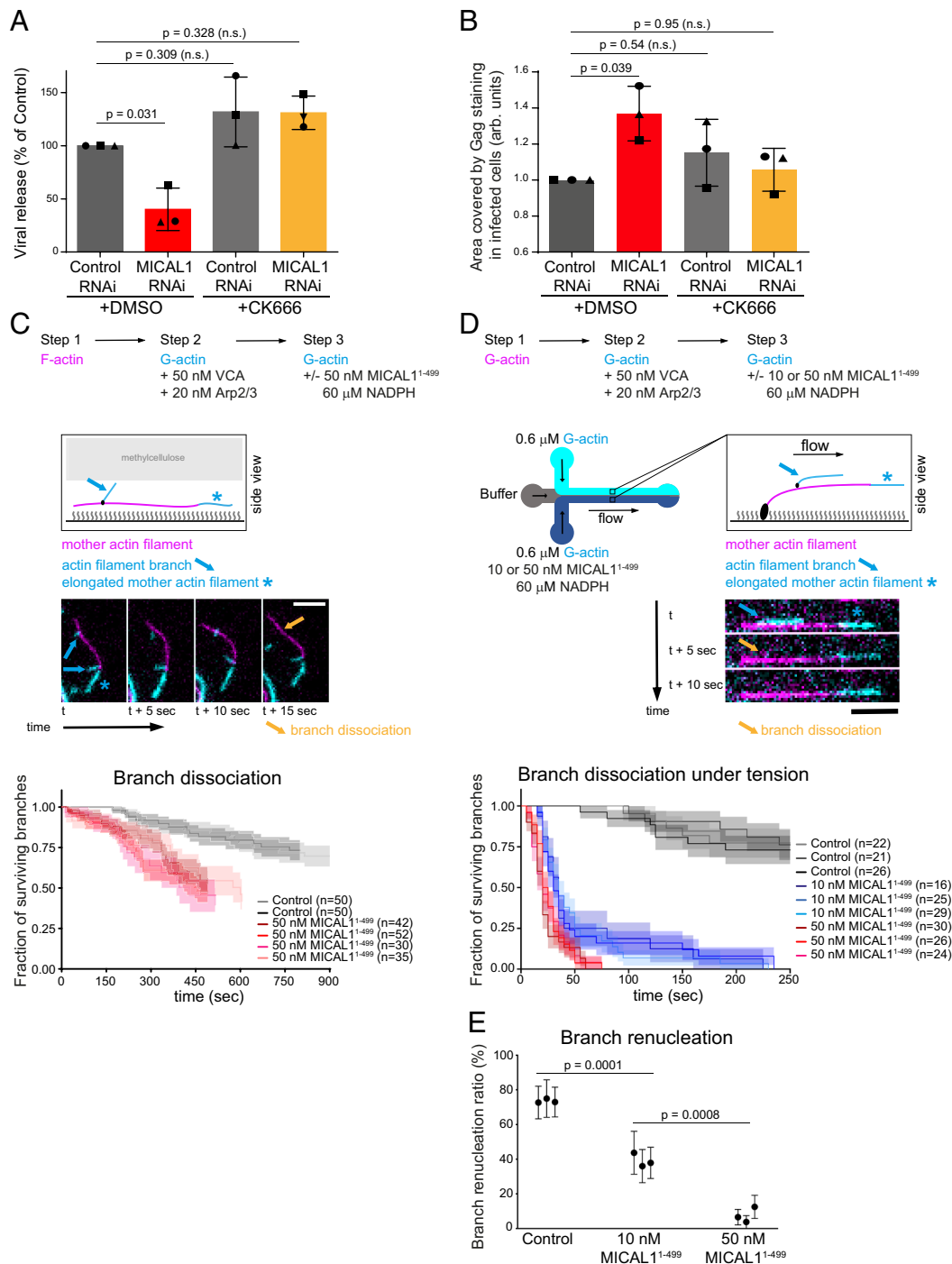
Fig. 5. Inhibiting branched-actin nucleation restores normal HIV-1 release in MICAL1-depleted cells, and MICAL1 exhibits debranching activity. (*A*) Quantification by Gag-p24 ELISA of HIV-1 release in Control and MICAL1-depleted HeLa cells, treated with either dimethyl sulfoxide (DMSO) or CK666 (75 µM). Results were normalized to control RNAi treated with DMSO conditions (set at 100%). Error bars represent SD calculated from three independent experiments, each done in triplicate. One-way ANOVA multiple comparisons. (*B*) Quantification of the area covered by Gag staining in infected cells (arbitrary units, arb.units.). Error bars represent SD calculated from three independent experiments. n = 185, 188, 206, and 185 cells analyzed for Control RNAi+DMSO, Control RNAi+CK666, MICAL1 RNAi+DMSO and MICAL1 RNAi+CK666 conditions, respectively. One-way ANOVA multiple comparisons. (*C*, *Top*) Schematic of branching and debranching experiment in an in vitro reconstitution assay using an open microchamber. (*Middle*) Fluorescence microscope image sequence, showing the dissociation (yellow arrow) of an actin filament branch (cyan+blue arrow) from its mother filament (magenta, and cyan+blue star). The time interval between images is 5 s. Filaments were monitored in the presence of 0.3 µM 10% ATTO-488 labeled G-actin (cyan)—causing all barbed ends to elongate—with or without 50 nM MICAL1[1-499] (active catalytic domain) and 60 µM NADPH. (Scale bar, 5 µm.) (*Bottom*) Fraction of remaining (undissociated) actin filament branches as a function of time, in the presence or absence of MICAL1[1-499] and NADPH. The shaded areas show the 65% CI. Between control (pooled repeats) and 50 nM (pooled repeats), *P* < 0.0001 (log-rank test). (*D*, *Top*) Schematic of the debranching experiment in an in vitro reconstitution assay using a microfluidics chamber. Filaments are exposed to different conditions (with or without MICAL1[1-499] and NADPH) side by side, in the same chamber. (*Middle*) The microscope image sequence shows the dissociation (yellow arrow) of an actin filament branch (cyan+blue arrow) from its mother filament (magenta, and cyan+blue star). The time interval between images is 5 s. (Scale bar, 5 µm.) (*Bottom*) Fraction of remaining (undissociated) actin filament branches as a function of time, under indicated conditions. Each curve shows the surviving fraction of different populations of n branches over time. In all these experiments, the average force on branch junctions was 0.32 (±0.03, SD) pN at t = 0 and increased at a rate of 0.00056 (±0.00011, SD) pN/s as the branches elongated over time. The shaded areas show the 65% CI. Between different concentrations (pooled repeats), *P* < 0.0001 (log-rank test). (*E*) Percentage of branches that renucleate after dissociating, in the presence of 60 µM NADPH and different concentrations of MICAL1[1-499]. Each data point corresponds to one experiment, monitoring, from left to right, n = 22, 16, 26, 16, 25, 29, 30, 26, 24 dissociated branches (same filament populations as in *D*). Error bars show binomial SD.

branch renucleation in microfluidics experiments (Fig. 5*E*). We found that the presence of MICAL1 efficiently prevented the renucleation of branches. Thus, our results reveal that MICAL1 has a debranching activity and regulates the dynamics of branched actin networks.

MICAL1 and Its Activator the GTPase Rab35 Function in the Same Pathway in HIV-1 Release. MICAL1 enzymatic activity is tightly regulated in cells. In cytokinesis, MICAL1 is recruited and activated at the ICB by the small GTPase Rab35 to locally depolymerize actin filaments (34). We thus investigated the potential role of Rab35 in HIV-1 release and, if so, whether it acts in the same pathway as MICAL1. We silenced Rab35 alone or together with MICAL1 using specific siRNAs in infected HeLa cells and measured viral release by WB (Fig. 6*A*). Depletion

of Rab35, alone or in combination with MICAL1, reduced released Gag-p24, as shown by WB quantifications (Fig. 6*A* and *SI Appendix,* Fig. S5*A*). Quantifications by Gag-p24-ELISA showed similar release defects after either MICAL1 depletion or Rab35 depletion (Fig. 6*B*). Importantly, no additive effect on viral release was observed when MICAL1 and Rab35 were codepleted (Fig. 6*B* and *SI Appendix,* Fig. S5*A*). Furthermore, as in MICAL1-depleted cells, the total area covered by budding regions was increased in Rab35-depleted cells (*SI Appendix,* Fig. S5*B* and quantified in Fig. 6*C*). Compared to either Rab35 or MICAL1 depletion alone, no further increase in the total area covered by budding regions was observed when Rab35 and MICAL1 were depleted together (*SI Appendix,* Fig. S5*B* and Fig. 6*C*). These results are consistent with the idea that MICAL1 and its activator Rab35 functions in the same pathway in HIV-1 release.
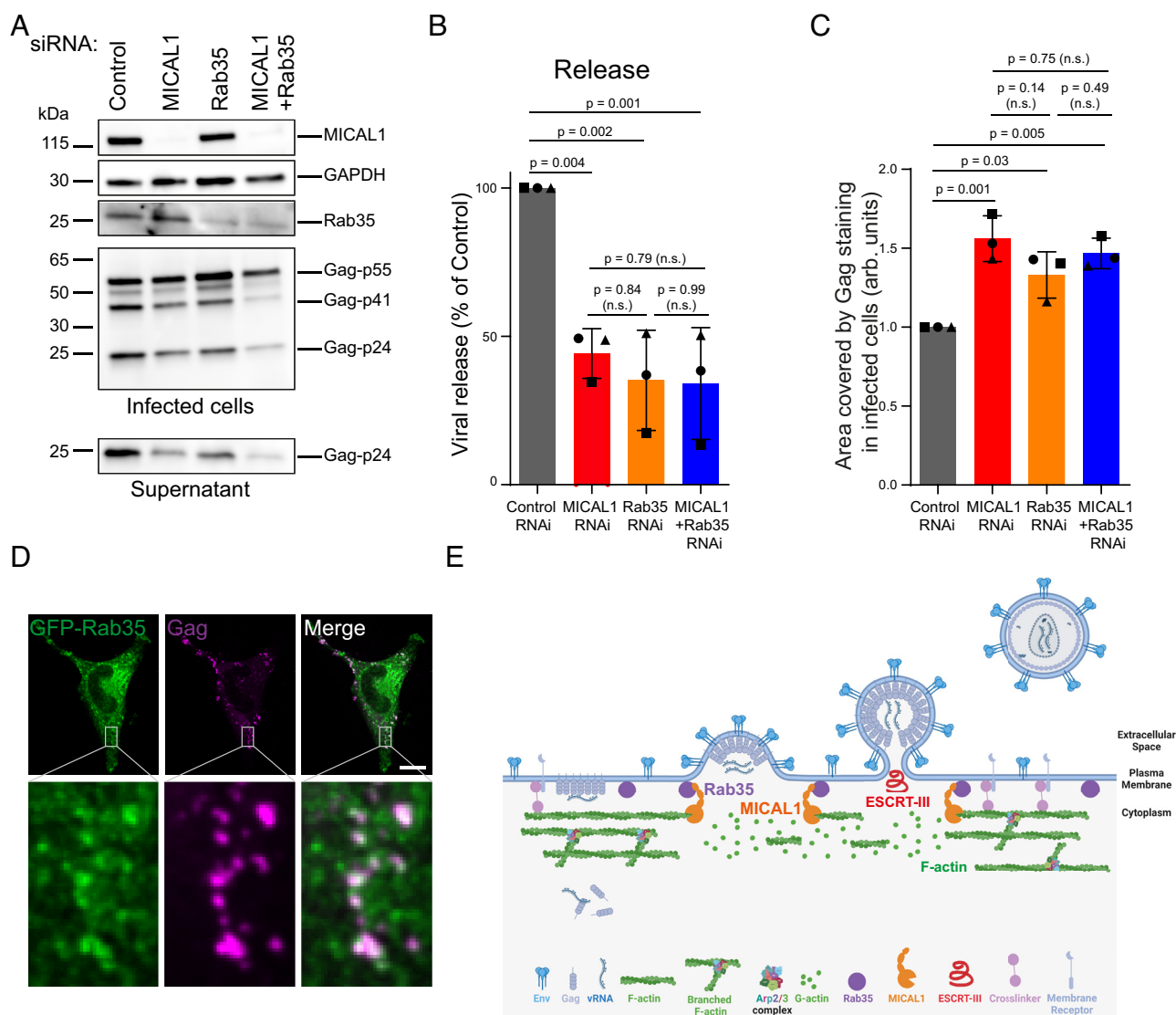

Fig. 6. MICAL1 and its activator the GTPase Rab35 act in the same pathway in HIV-1 release. (*A*) WB analysis of HIV-1 Gag products in infected HeLa cells treated with indicated siRNAs (panels Infected cells) and corresponding supernatants (panel Supernatant). Loading control: GAPDH. Equal volumes of cell and supernatant samples were loaded. This experiment was repeated at least three times independently with similar results. (*B*) Quantification by Gag-p24 ELISA of HIV-1 release in infected HeLa cells treated with either Control, MICAL1, Rab35, or MICAL1+Rab35 siRNAs. Results were normalized to control RNAi conditions (set at 100%). Error bars represent SD calculated from three independent experiments, each done in triplicate. One-way ANOVA multiple comparisons. (*C*) Quantification of the area covered by Gag staining in infected cells (arbitrary units, arb.units.). Error bars represent SD calculated from three independent experiments. n = 126, 133, 122, and 131 cells analyzed for Control RNAi, MICAL1 RNAi, Rab35 RNAi, and MICAL1+Rab35 RNAi conditions, respectively. One-way ANOVA multiple comparisons. (*D*) Spinning disk confocal images of genome-edited HeLa cells that express endogenous Rab35 tagged with GFP and stained with anti-Gag (magenta) antibody and GFP-Booster nanobody (green) after infection. (Scale bars, 10 μm.) (*E*) Model for F-actin clearance by MICAL1 at budding site during HIV-1 budding. We propose that Rab35 at HIV-1 budding sites activates the redox enzyme MICAL1, which locally disassembles cortical F-actin through its depolymerizing and debranching activities. This is required for complete budding and normal ESCRT-III recruitment and thereby promotes viral release.

We next investigated whether Rab35 localized at HIV-1 budding regions. Using spinning disk confocal microscopy in a cell line where Rab35 is tagged with GFP at the endogenous locus (50), we detected the presence of Rab35 in 90% of the budding regions (Fig. 6D, n = 277 budding regions in nine infected cells, and *SI Appendix,* Fig. S5C). As a control, we used the GTPase Rab11 that does not interact with MICAL1 (51) and did not detect it at budding regions (*SI Appendix,* Fig. S5D). Altogether, we conclude that Rab35 localizes at viral budding sites, and we propose that Rab35 functions at this location to allow proper HIV-1 budding and release.

Discussion

Here, we report that the enzyme MICAL1 controls F-actin clearance at budding sites to promote HIV-1 budding and release (Fig. 6E). In the absence of MICAL1, F-actin remains underneath budding sites, CHMP4B recruitment is delayed, virus particles accumulate at the plasma membrane and HIV-1 release is reduced. Mechanistically, MICAL1 depletion affects the budding process, since incompletely budded particles accumulate at the plasma membrane in the absence of MICAL1.

HIV-1 assembles and buds from areas of the plasma membrane with reduced F-actin levels [(22) and this study]. How could the abnormal presence of F-actin at budding sites observed upon MICAL1 depletion impact viral budding? One possibility is that F-actin clearance by MICAL1 promotes full Gag-mediated membrane deformation up to the point enabling the recruitment of ESCRT-III. In noninfected cells, membrane–cytoskeleton interactions affect plasma membrane mechanics and tension (15, 17, 52). In particular, proteins linking the plasma membrane to the actin cortex, such as Ezrin, Radixin, Moesin (ERMs), were shown to control membrane deformation (14) and have been implicated in the HIV-1 cycle (53–55). High levels of F-actin at budding sites in the absence of MICAL1 may thus enhance ERM localization at these sites thereby preventing membrane deformation. Alternatively, these abnormal actin levels might impact on the localization of factors that play an active role in membrane deformation, such as the BAR-domain protein IRSp53 and Angiomotin (AMOT) (40, 41). Interestingly, the depletion of either IRSp53 or AMOT induces viral bud arrest at half completion, in a "half-moon" shape (40, 41), as observed upon MICAL1 depletion. It is thus possible that MICAL1 acts together with IRSp53/AMOT or in parallel in the same step of viral budding.

We found that MICAL1 depletion reduces HIV-1 release in two adherent cell lines, HeLa cells and monocyte-derived macrophages THP-1. However, we did not observe release defects in T lymphocytes upon MICAL1 depletion. Nevertheless, we found that budding viruses are present mainly in plasma membrane areas where the F-actin level is reduced in both Jurkat T cells and primary activated CD4+ T cells, similarly to HeLa cells. One possibility is that MICAL1 requirement for actin disassembly at budding sites is different in adherent vs. nonadherent cells. Alternatively, the MICAL family comprises three members, MICAL1, MICAL2, and MICAL3, and have all been shown to induce F-actin depolymerization in vitro (36, 56). These enzymes could thus play a redundant role in viral budding in infected T cells.

The fact that we were able to rescue the release defects in MICAL1-depleted cells by inhibiting Arp2/3 suggests that MICAL1 promotes the disassembly of branched actin during viral budding. Thus far, it is well established that MICAL1-dependent oxidation of linear actin filaments can induce their rapid depolymerization in vitro (34, 57–59). Here, we found that MICAL1, in addition, has a debranching activity by inducing the dissociation of actin filament branches from their mother filament. Our in vitro assays also revealed MICAL1's ability to prevent the renucleation of dissociated branches, which is likely to play a role in situations of rapid filament turnover, as in the cell cortex. Recently, MICAL2 was found to promote the disassembly of the branched actin tails that propel vaccinia viruses within cells (60). It was shown that MICAL2 can oxidize Arp3B (60), but whether MICAL2 has a direct debranching activity has not been investigated. Since the catalytic domains of MICAL proteins are similar, it is likely that the debranching activity of MICAL1 that we observed in vitro is the consequence of the direct oxidation of the Arp2/3 complex. Further investigations are required to determine whether the oxidation of actin subunits in contact with the Arp2/3 complex at the branch junction also plays a role in actin branch dissociation.

A recent study reported that branched actin disassembly plays an early role during viral assembly (22). Indeed, infected T cells treated with CK666 favored the initial formation of Gag clusters at the plasma membrane, thereby increasing particle production. Consistently, in vitro experiments indicate that low F-actin density promotes the initiation of Gag clustering on model membranes (22). It was further shown that Gag recruits the Arp2/3 inhibitory protein Arpin during viral assembly (22). An interesting possibility is that Arpin and MICAL1 function successively in the different steps of viral particle formation.

Our results indicate that MICAL1 acts locally at budding sites to depolymerize F-actin. However, we were unable to detect MICAL1 at budding sites using confocal spinning disk microscopy. This is likely due to the low amounts of MICAL1 present at the budding sites, that would require more sensitive approaches to be detected. Superresolution microscopy, such as single-molecule localization microscopy (SMLN), could help for localizing MICAL1 at budding sites, as it has been successfully used for IRSp53 (41). Another possibility is that MICAL1 recruitment is too dynamic to be captured in fixed samples. Although technically challenging, live-cell microscopy on cells infected with tagged versions of the virus could be used to observe transient recruitment of MICAL1 at budding sites.

Besides being recruited at the right place at the right time, MICAL1 must be activated. Since it exhibits a strong actin depolymerizing activity, MICAL1 exists in an autoinhibited conformation and either Plexin receptors or Rab GTPase binding to its C-terminal region releases this inhibition (57, 61–65). We previously demonstrated that the GTPase Rab35 interacts with this region, activates the enzymatic activity of MICAL1 in vitro, and determines its localization at the ICB during cytokinesis (34). During viral assembly, Gag creates its own lipid nanodomains enriched in PtdIns(4,5)P2 at the plasma membrane (66–70). Interestingly, Rab35 contains an evolutionarily conserved polybasic C-terminal tail which facilitates its interaction with PtdIns(4,5)P2 and PtdIns(3,4,5)P3 at the plasma membrane (71, 72). In addition, Rab35 is incorporated into virions (73). However, its potential role in assembly, budding, or release has not been investigated. Here, we show that Rab35 localizes at budding sites and promotes HIV-1 release. Our data further suggest that Rab35 and MICAL1 act in the same pathway in viral release. Thus, we propose that the Rab35/MICAL1 pathway, which locally clears F-actin at the plasma membrane, is used both for cytokinesis and viral budding.

In conclusion, we report a role of actin oxidation by MICAL1 in the late steps of the HIV-1 cycle and reveal a connection between oxidoreduction and viral budding. This raises the possibility that other enveloped viruses use similar MICAL-dependent strategies to remodel the cortical actin in order to promote viral budding and release.

Materials and Methods

Please see *SI Appendix, Supplementary Methods and Information* for information regarding Cell cultures, Antibodies and plasmids, WB, Gag-p24 ELISA, Infectivity analysis, Purification of viruses, Cell viability assay, TEM, Correlative light and SEM, Immunofluorescence and image acquisition with spinning disk confocal microscopy, Immunofluorescence and image acquisition with 3D STORM, Image and data analysis, TIRF microscopy, Immunoprecipitation, Yeast two-hybrid experiments, and In vitro single actin filament assays.

siRNA Transfections. For silencing experiments, HeLa cells were transfected with 25 nM siRNAs (siControl, siMICAL1, siMICAL1#2, siRab35) for 5 d using Lipofectamine RNAiMAX (Invitrogen), following the manufacturer's instructions.

For silencing experiments, THP-1 cells were transfected with 50 nM siRNAs using Lipofectamine RNAiMAX. The day after, phorbol 12-myristate 13-acetate (PMA, Sigma) at 167 ng/mL was added to the culture medium to differentiate THP-1 cells in macrophages. Forty-eight hours later, a second siRNA transfection was done using Hiperfect (Qiagen).

siRNAs against Luciferase (used as control, 5′CGUACGCGGAAUACUUCGA[dU][dU]3′), MICAL1 (5′GAGUCCACGUCUCCGAUUU[dU][dU]3′) (34), MICAL1#2 (5′CUCGGUGCUAAGAAGUUCU[dU][dU]3′) (74), and Rab35 (5′GCUCACGAAG AACAGUAAA[dU][dU]3′) (75) were synthetized by Sigma.

Virus Production. Viral particles were produced by Turbofect (Invitrogen) transfection of 293 T cells with HIV-1 proviral DNA (NL4-3 strain) along with a VSV-G expression vector, following manufacturer instructions. Forty-eight hours after transfection, supernatants containing the viral particles were collected and filtered with a 0.45-μm filter to remove cell debris. The amounts of viruses produced were quantified by Gag-p24 ELISA.

Infection Experiments. Seventy-two hours after siRNA transfection, HeLa cells were infected with the HIV-1 strain NL4-3 (NIH AIDS Research and Reference Reagent Program, Division of AIDS, NIAID) pseudotyped with the vesicular stomatitis virus G glycoprotein (NL4-3-VSVG). Sixteen hours after infection, the viral input was removed. Twenty-four hours after, both viruses released in the supernatant and infected cells were analyzed by Western-blot and Gag-p24 ELISA. For the kinetics of Gag-p24 release in the supernatant of infected HeLa cells, viral input was removed twenty-four hours postinfection, and fresh medium was added. From this time point onward, viral supernatants were collected at 4 – 6 – 8 and 24 h to perform Gag-p24 measurements using ELISA.

Monocyte-derived macrophages THP-1 cells were infected with HIV-1 strain NL4-3-VSVG. Sixteen hours after infection, viral input was removed. Forty-eight hours after, both viruses released in the supernatant and infected cells were analyzed by Western-blot and Gag-p24 ELISA. Jurkat T cells and activated primary CD4+ T cells were infected with the HIV-1 strain NL4-3-VSVG. Sixteen hours after infection, the viral input was removed. Twenty-four

hours after, infected cells were fixed and analyzed by confocal spinning disk microscopy.

Statistics. All plots and statistical tests were performed using GraphPad Prism software. The presented values are displayed as mean ± SD from at least three independent experiments and the test used is indicated in the figure legends. In all statistical tests, *P*-value > 0.05 was considered as nonsignificant. *P*-values are indicated in the figures.

Data, Materials, and Software Availability. All study data are included in the article and/or *SI Appendix*.

Author affiliations: [a]Membrane Traffic and Cell Division Unit, Institut Pasteur, Université Paris Cité, CNRS UMR3691, Paris F-75015, France; [b]Virology department, Virus and Immunity Lab, Institut Pasteur, Université Paris Cité, Paris F-75015, France; [c]Université Paris Cité, CNRS, Institut Jacques Monod, Paris F-75013, France; [d]Institut Pasteur, Université Paris Cité, Photonic Bio-Imaging Unit, Centre de Ressources et Recherches Technologiques (UTechS-PBI, C2RT), Paris F-75015, France; [e]Institut Pasteur, Université Paris Cité, Ultrastructural BioImaging, Paris F-75015, France; [f]Université de Strasbourg, Institut de Biologie Moléculaire et Cellulaire, Architecture et Réactivité de l'ARN, CNRS UPR9002, Strasbourg F-67084, France; and [g]Institut de Génétique et de Biologie Moléculaire et Cellulaire (IGBMC), Department of Integrated Structural Biology, CNRS UMR 7104, Inserm U 1258, University of Strasbourg, Illkirch F-67404, France

1. D. G. Demirov, J. M. Orenstein, E. O. Freed, The late domain of human immunodeficiency virus type 1 p6 promotes virus release in a cell type-dependent manner. *J. Virol.* **76**, 105–117 (2002).
2. J. E. Garrus *et al.*, Tsg101 and the vacuolar protein sorting pathway are essential for HIV-1 budding. *Cell* **107**, 55–65 (2001).
3. J. Martin-Serrano, T. Zang, P. D. Bieniasz, HIV-1 and Ebola virus encode small peptide motifs that recruit Tsg101 to sites of particle assembly to facilitate egress. *Nat. Med.* **7**, 1313–1319 (2001).
4. L. VerPlank *et al.*, Tsg101, a homologue of ubiquitin-conjugating (E2) enzymes, binds the L domain in HIV type 1 Pr55(Gag). *Proc. Natl. Acad. Sci. U.S.A.* **98**, 7724–7729 (2001).
5. U. K. von Schwedler *et al.*, The protein network of HIV budding. *Cell* **114**, 701–713 (2003).
6. J. G. Carlton, J. Martin-Serrano, Parallels between cytokinesis and retroviral budding: A role for the ESCRT machinery. *Science* **316**, 1908–1912 (2007).
7. E. Morita *et al.*, Human ESCRT and ALIX proteins interact with proteins of the midbody and function in cytokinesis. *EMBO J.* **26**, 4215–4227 (2007).
8. M. Vietri, M. Radulovic, H. Stenmark, The many functions of ESCRTs. *Nat. Rev. Mol. Cell Biol.* **21**, 25–42 (2020).
9. J. McCullough, A. Frost, W. I. Sundquist, Structures, functions, and dynamics of ESCRT-III/Vps4 membrane remodeling and fission complexes. *Annu. Rev. Cell Dev. Biol.* **34**, 85–109 (2018).
10. E. J. Scourfield, J. Martin-Serrano, Growing functions of the ESCRT machinery in cell biology and viral replication. *Biochem. Soc. Trans.* **45**, 613–634 (2017).
11. G. Lerner, N. Weaver, B. Anokhin, P. Spearman, Advances in HIV-1 assembly. *Viruses* **14** (2022).
12. W. I. Sundquist, H. G. Krausslich, HIV-1 assembly, budding, and maturation. *Cold Spring Harb. Perspect Med.* **2**, a006924 (2012).
13. E. O. Freed, HIV-1 assembly, release and maturation. *Nat. Rev. Microbiol.* **13**, 484–496 (2015).
14. P. Chugh, E. K. Paluch, The actin cortex at a glance. *J. Cell Sci.* **131** (2018).
15. M. Kelkar, P. Bohec, G. Charras, Mechanics of the cellular actin cortex: From signalling to shape change. *Curr. Opin. Cell Biol.* **66**, 69–78 (2020).
16. A. M. Gautreau, F. E. Fregoso, G. Simanov, R. Dominguez, Nucleation, stabilization, and disassembly of branched actin networks. *Trends Cell Biol.* **32**, 421–432 (2022).
17. R. S. Kadzik, K. E. Homa, D. R. Kovar, F-actin cytoskeleton network self-organization through competition and cooperation. *Annu. Rev. Cell Dev. Biol.* **36**, 35–60 (2020).
18. C. Jolly, I. Mitar, Q. J. Sattentau, Requirement for an intact T-cell actin and tubulin cytoskeleton for efficient assembly and spread of human immunodeficiency virus type 1. *J. Virol.* **81**, 5547–5560 (2007).
19. G. Audoly, M. R. Popoff, P. Gluschankof, Involvement of a small GTP binding protein in HIV-1 release. *Retrovirology* **2**, 48 (2005).
20. M. Gladnikoff, E. Shimoni, N. S. Gov, I. Rousso, Retroviral assembly and budding occur through an actin-driven mechanism. *Biophys. J.* **97**, 2419–2428 (2009).
21. L. A. Carlson *et al.*, Cryo electron tomography of native HIV-1 budding sites. *PLoS Pathog.* **6**, e1001173 (2010).
22. R. Dibsy, E. Bremaud, J. Mak, C. Favard, D. Muriaux, HIV-1 diverts cortical actin for particle assembly and release. *Nat. Commun.* **14**, 6945 (2023).
23. S. A. Rahman *et al.*, Investigating the role of F-actin in human immunodeficiency virus assembly by live-cell microscopy. *J. Virol.* **88**, 7904–7914 (2014).
24. S. Stauffer *et al.*, The nucleocapsid domain of Gag is dispensable for actin incorporation into HIV-1 and for association of viral budding sites with cortical F-actin. *J. Virol.* **88**, 7893–7903 (2014).
25. T. Serrano, S. Fremont, A. Echard, Get in and get out: Remodeling of the cellular actin cytoskeleton upon HIV-1 infection. *Biol. Cell* **115**, e2200085 (2023), 10.1111/boc.202200085.

26. D. Dambournet et al., Rab35 GTPase and OCRL phosphatase remodel lipids and F-actin for successful cytokinesis. Nat. Cell Biol. 13, 981–988 (2011).
27. J. A. Schiel et al., FIP3-endosome-dependent formation of the secondary ingression mediates ESCRT-III recruitment during cytokinesis. Nat. Cell Biol. 14, 1068–1078 (2012).
28. S. Fremont, A. Echard, Membrane traffic in the late steps of cytokinesis. Curr. Biol. 28, R458–R470 (2018).
29. R. Kumar et al., DENND2B activates Rab35 at the intercellular bridge, regulating cytokinetic abscission and tetraploidy. Cell Rep. 42, 112795 (2023).
30. N. V. G. Iannantuono, G. Emery, Rab11FIP1 maintains Rab35 at the intercellular bridge to promote actin removal and abscission. J. Cell Sci. 134 (2021).
31. S. J. Terry, F. Dona, P. Osenberg, J. G. Carlton, U. S. Eggert, Capping protein regulates actin dynamics during cytokinetic midbody maturation. Proc. Natl. Acad. Sci. U.S.A. 115, 2138–2143 (2018).
32. J. Bai et al., Actin reduction by MsrB2 is a key component of the cytokinetic abscission checkpoint and prevents tetraploidy. Proc. Natl. Acad. Sci. U.S.A. 117, 4169–4179 (2020).
33. C. Addi, J. Bai, A. Echard, Actin, microtubule, septin and ESCRT filament remodeling during late steps of cytokinesis. Curr. Opin. Cell Biol. 50, 27–34 (2018).
34. S. Fremont et al., Oxidation of F-actin controls the terminal steps of cytokinesis. Nat. Commun. 8, 14528 (2017).
35. C. Rouyere, T. Serrano, S. Fremont, A. Echard, Oxidation and reduction of actin: Origin, impact in vitro and functional consequences in vivo. Eur. J. Cell Biol. 101, 151249 (2022).
36. L. T. Alto, J. R. Terman, MICALs. Curr. Biol. 28, R538–R541 (2018).
37. S. S. Giridharan, S. Caplan, MICAL-family proteins: Complex regulators of the actin cytoskeleton. Antioxid. Redox Signal 20, 2059–2073 (2014).
38. M. A. Vanoni, Structure-function studies of MICAL, the unusual multidomain flavoenzyme involved in actin cytoskeleton dynamics. Arch. Biochem. Biophys. 632, 118–141 (2017).
39. S. Rajan, J. R. Terman, E. Reisler, MICAL-mediated oxidation of actin and its effects on cytoskeletal and cellular dynamics. Front. Cell Dev. Biol. 11, 1124202 (2023).
40. G. Mercenne, S. L. Alam, J. Arii, M. S. Lalonde, W. I. Sundquist, Angiomotin functions in HIV-1 assembly and budding. Elife 4 (2015).
41. K. Inamdar et al., Full assembly of HIV-1 particles requires assistance of the membrane curvature factor IRSp53. Elife 10 (2021).
42. D. G. Demirov, A. Ono, J. M. Orenstein, E. O. Freed, Overexpression of the N-terminal domain of TSG101 inhibits HIV-1 budding by blocking late domain function. Proc. Natl. Acad. Sci. U.S.A. 99, 955–960 (2002).
43. C. Addi et al., The Flemmingsome reveals an ESCRT-to-membrane coupling via ALIX/syntenin/ syndecan-4 required for completion of cytokinesis. Nat. Commun. 11, 1941 (2020).
44. N. Jouvenet, P. D. Bieniasz, S. M. Simon, Imaging the biogenesis of individual HIV-1 virions in live cells. Nature 454, 236–240 (2008).
45. N. Jouvenet, M. Zhadina, P. D. Bieniasz, S. M. Simon, Dynamics of ESCRT protein recruitment during retroviral assembly. Nat. Cell Biol. 13, 394–401 (2011).
46. E. E. Grintsevich et al., Catastrophic disassembly of actin filaments via Mical-mediated oxidation. Nat. Commun. 8, 2183 (2017).
47. A. Jegou, M. F. Carlier, G. Romet-Lemonne, Microfluidics pushes forward microscopy analysis of actin dynamics. Bioarchitecture 1, 271–276 (2011).
48. F. Ghasemi et al., Regeneration of actin filament branches from the same Arp2/3 complex. Sci. Adv. 10, eadj7681 (2024).
49. N. G. Pandit et al., Force and phosphate release from Arp2/3 complex promote dissociation of actin filament branches. Proc. Natl. Acad. Sci. U.S.A. 117, 13519–13528 (2020).
50. C. Cauvin et al., Rab35 GTPase triggers switch-like recruitment of the lowe syndrome lipid phosphatase OCRL on newborn endosomes. Curr. Biol. 26, 120–128 (2016).
51. M. Fukuda, E. Kanno, K. Ishibashi, T. Itoh, Large scale screening for novel rab effectors reveals unexpected broad Rab binding specificity. Mol. Cell Proteomics 7, 1031–1042 (2008).
52. A. G. Clark, O. Wartlick, G. Salbreux, E. K. Paluch, Stresses at the cell surface during animal cell morphogenesis. Curr. Biol. 24, R484–R494 (2014).
53. M. Barrero-Villar et al., Moesin is required for HIV-1-induced CD4-CXCR4 interaction, F-actin redistribution, membrane fusion and viral infection in lymphocytes. J. Cell Sci. 122, 103–113 (2009).
54. N. H. Roy, J. Lambele, M. Chan, M. Symeonides, M. Thali, Ezrin is a component of the HIV-1 virological presynapse and contributes to the inhibition of cell-cell fusion. J. Virol. 88, 7645–7658 (2014).
55. H. Kamiyama et al., Role of ezrin phosphorylation in HIV-1 replication. Front. Microbiol. 9, 1912 (2018).
56. H. Wu, H. G. Yesilyurt, J. Yoon, J. R. Terman, The MICALs are a family of f-actin dismantling oxidoreductases conserved from Drosophila to humans. Sci. Rep. 8, 937 (2018).
57. R. J. Hung et al., Mical links semaphorins to F-actin disassembly. Nature 463, 823–827 (2010).
58. R. J. Hung, C. W. Pak, J. R. Terman, Direct redox regulation of F-actin assembly and disassembly by Mical. Science 334, 1710–1713 (2011).
59. S. Rajan et al., Disassembly of bundled F-actin and cellular remodeling via an interplay of Mical, cofilin, and F-actin crosslinkers. Proc. Natl. Acad. Sci. U.S.A. 120, e2309955120 (2023).
60. C. Galloni et al., MICAL2 enhances branched actin network disassembly by oxidizing Arp3B-containing Arp2/3 complexes. J. Cell Biol. 220 (2021).
61. E. F. Schmidt, S. O. Shim, S. M. Strittmatter, Release of MICAL autoinhibition by semaphorin-plexin signaling promotes interaction with collapsin response mediator protein. J. Neurosci. 28, 2287–2297 (2008).
62. J. R. Terman, T. Mao, R. J. Pasterkamp, H. H. Yu, A. L. Kolodkin, MICALs, a family of conserved flavoprotein oxidoreductases, function in plexin-mediated axonal repulsion. Cell 109, 887–900 (2002).
63. S. S. Giridharan, J. L. Rohn, N. Naslavsky, S. Caplan, Differential regulation of actin microfilaments by human MICAL proteins. J. Cell Sci. 125, 614–624 (2012).
64. T. Vitali, E. Maffioli, G. Tedeschi, M. A. Vanoni, Properties and catalytic activities of MICAL1, the flavoenzyme involved in cytoskeleton dynamics, and modulation by its CH, LIM and C-terminal domains. Arch. Biochem. Biophys. 593, 24–37 (2016).
65. A. Rai et al., bMERB domains are bivalent Rab8 family effectors evolved by gene duplication. Elife 5 (2016).
66. V. Chukkapalli, I. B. Hogue, V. Boyko, W. S. Hu, A. Ono, Interaction between the human immunodeficiency virus type 1 Gag matrix domain and phosphatidylinositol-(4,5)-bisphosphate is essential for efficient gag membrane binding. J. Virol. 82, 2405–2417 (2008).
67. V. Chukkapalli, A. Ono, Molecular determinants that regulate plasma membrane association of HIV-1 Gag. J. Mol. Biol. 410, 512–524 (2011).
68. A. Ono, S. D. Ablan, S. J. Lockett, K. Nagashima, E. O. Freed, Phosphatidylinositol (4,5) bisphosphate regulates HIV-1 Gag targeting to the plasma membrane. Proc. Natl. Acad. Sci. U.S.A. 101, 14889–14894 (2004).
69. C. Favard et al., HIV-1 Gag specifically restricts PI(4,5)P2 and cholesterol mobility in living cells creating a nanodomain platform for virus assembly. Sci. Adv. 5, eaaw8651 (2019).
70. P. Sengupta et al., A lipid-based partitioning mechanism for selective incorporation of proteins into membranes of HIV particles. Nat. Cell Biol. 21, 452–461 (2019).
71. W. D. Heo et al., PI(3,4,5)P3 and PI(4,5)P2 lipids target proteins with polybasic clusters to the plasma membrane. Science 314, 1458–1461 (2006).
72. K. Klinkert, A. Echard, Rab35 GTPase: A central regulator of phosphoinositides and F-actin in endocytic recycling and beyond. Traffic 17, 1063–1077 (2016), 10.1111/tra.12422.
73. K. Dicker, A. I. Jarvelin, M. Garcia-Moreno, A. Castello, The importance of virion-incorporated cellular RNA-Binding Proteins in viral particle assembly and infectivity. Semin. Cell Dev. Biol. 111, 108–118 (2021).
74. W. Deng et al., MICAL1 controls cell invasive phenotype via regulating oxidative stress in breast cancer cells. BMC Cancer 16, 489 (2016).
75. I. Kouranti, M. Sachse, N. Arouche, B. Goud, A. Echard, Rab35 regulates an endocytic recycling pathway essential for the terminal steps of cytokinesis. Curr. Biol. 16, 1719–1725 (2006).